Bulletin of Engineering Geology and the Environment (2019) 78:4919–4930
https://doi.org/10.1007/s10064-018-01432-8

ORIGINAL PAPER

Investigation into the triggering mechanism of loess landslides in the south Jingyang platform, Shaanxi province

Zhao Duan[1,2,3] · Wen-Chieh Cheng[3] · Jiang-Bing Peng[4,5] · Qi-Yao Wang[6] · Wei Chen[1]

Received: 2 June 2018 / Accepted: 24 November 2018 / Published online: 19 December 2018

Abstract

Loess landslide incidents have resulted in significant economic losses and human casualties in Northwest China. To investigate the triggering mechanism of such loess landslides in the south Jingyang platform, Shaanxi province, an area which is subject to loess landslides, we performed a series of field measurements for loess landslide LD37 and also undertook laboratory. Comparisons between the field measurements of LD37 and the results of the constant shear drained (CSD) triaxial test indicate that the seepage from irrigation-water infiltration triggered the loess landslides in the study area where the initiation of the local sliding surfaces was linked to gentle stratum erosion and their subsequent development was because of excessive stratum erosion. The development of slow–rapid strain cycles in the ε–p' plot from the CSD triaxial test results indicates that loess landslides are a feature of progressive failure of the loess slope. Preventive measures to reduce irrigation-water infiltration into loess slopes should be taken to prevent similar incidents from recurring in the future.

Keywords Loess landslide · Jingyang platform · Agricultural irrigation · Stratum erosion

Introduction

Landslide has been assessed to be the most common geohazard associated with the urbanization process of rapidly expanding cities in Northwest China despite the use of several ground improvement methods (Shen et al. 2017; Wang et al. 2018a, b; Cheng et al. 2018b, c, d). The Loess Plateau, which covers almost all of Shaanxi province, Northwest China, is susceptible to landslide occurrences (Derbyshire et al. 1994; Derbyshire 2001; Zhou et al. 2002; Xu et al. 2007; Zhang et al. 2009; Zhang and Liu 2010; Wang et al. 2014; Peng et al. 2015; Zhuang et al. 2017; Zhang et al. 2017; Liu et al. 2018; Qiu et al. 2017, 2018). The well-developed joints and/or fractures in the loess provide additional seepage paths for either rainwater or irrigation water to infiltrate into the slope (Du et al. 2014a, b). Stratum erosion occurs when the seepage force is greater than the shear strength of the loess. This stratum erosion, particularly at the toe of the slope, not only leads to a downwards movement of the slope, but also initiates local sliding surfaces that may progressively develop into a global failure phenomenon. These local sliding surfaces could develop further and evolve into a global sliding surface when subjected to a stratum erosion of greater severity, thereby increasing the potential of loess landslide (Zhang et al. 2013, 2014). The raising of the phreatic surface plays an additional and crucial role in triggering loess landslides. Raising of the phreatic surface is subjected to many influencing factors, such as irrigation-water infiltration, domestic groundwater withdrawal, extreme climate, among others.

✉ Wen-Chieh Cheng
w-c.cheng@xauat.edu.cn

[1] College of Geology and Environment, Xi'an University of Science and Technology, Xi'an 710054, China

[2] Shandong Provincial Key Laboratory of Depositional Mineralization & Sedimentary Minerals, Shandong University of Science and Technology, Qingdao 266590, Shandong, China

[3] Shaanxi Key Laboratory of Geotechnical and Underground Space Engineering, School of Civil Engineering, Xi'an University of Architecture and Technology, Xi'an 710055, China

[4] School of Geology Engineering and Geomatics, Chang'an University, Xi'an 710054, China

[5] Key Laboratory of Western Mineral Resources and Geological Engineering of Ministry of Education, Chang'an University, Xi'an 710054, China

[6] School of Civil Engineering, Chang'an University, Xi'an 710054, China

The south Jingyang platform, located in Shaanxi province, is considered to be one of the world's most representative landslide-prone areas, with 62 severe loess landslides recorded since agricultural irrigation began in 1976. These loess landslides resulted in significant economic losses and human casualties (Lai et al. 2016, 2017; Cheng et al. 2017a, b, 2018a). Irrigation activities are necessary in Northwest China to enable the conversion of the natural loess into farmland in the very dry climate characteristic of the region. However, irrigation has a significant influence on phreatic surface variation (Shen and Xu 2011; Xu et al. 2012, 2014, 2016; Shen et al. 2013; Wu et al. 2015, 2016, 2017; Zhao et al. 2016; Zhang and Wang 2018). As phreatic surface variation is also subjected to many other influencing factors, the typical pattern of water pressure in this area is rather complex. Many earlier studies reported that the pattern of water pressure can be directly linked to the loess landslide incidents, but these studies did not take other influencing factors into account. Additionally, because of a lack of comparisons between field measurements and laboratory test results with complex real phenomena, a shared interpretation of the triggering mechanism of the loess landslides in the south Jingyang platform is still not available (Fell et al. 2007).

The objectives of this study are: (1) to introduce the types and characteristics of loess landslides in the south Jingyang platform, specifically for landslide LD37, (2) to analyze the field measurements of LD37 (Peng et al. 2017, 2018) in the light of results from constant shear drained (CSD) triaxial test results, and (3) to reveal the triggering mechanism of loess landslide incidents by exploring in depth the data from the comparisons of the CSD triaxial tests results and the field measurements with real phenomena.

Loess landslides in south Jingyang platform

Materials

The geological profile for the southern Loess Plateau and plan view of the study area are shown in Fig. 1. The geology primarily consists of loess deposit, underlain by silty clay deposit with occasional interbedded sand layers.

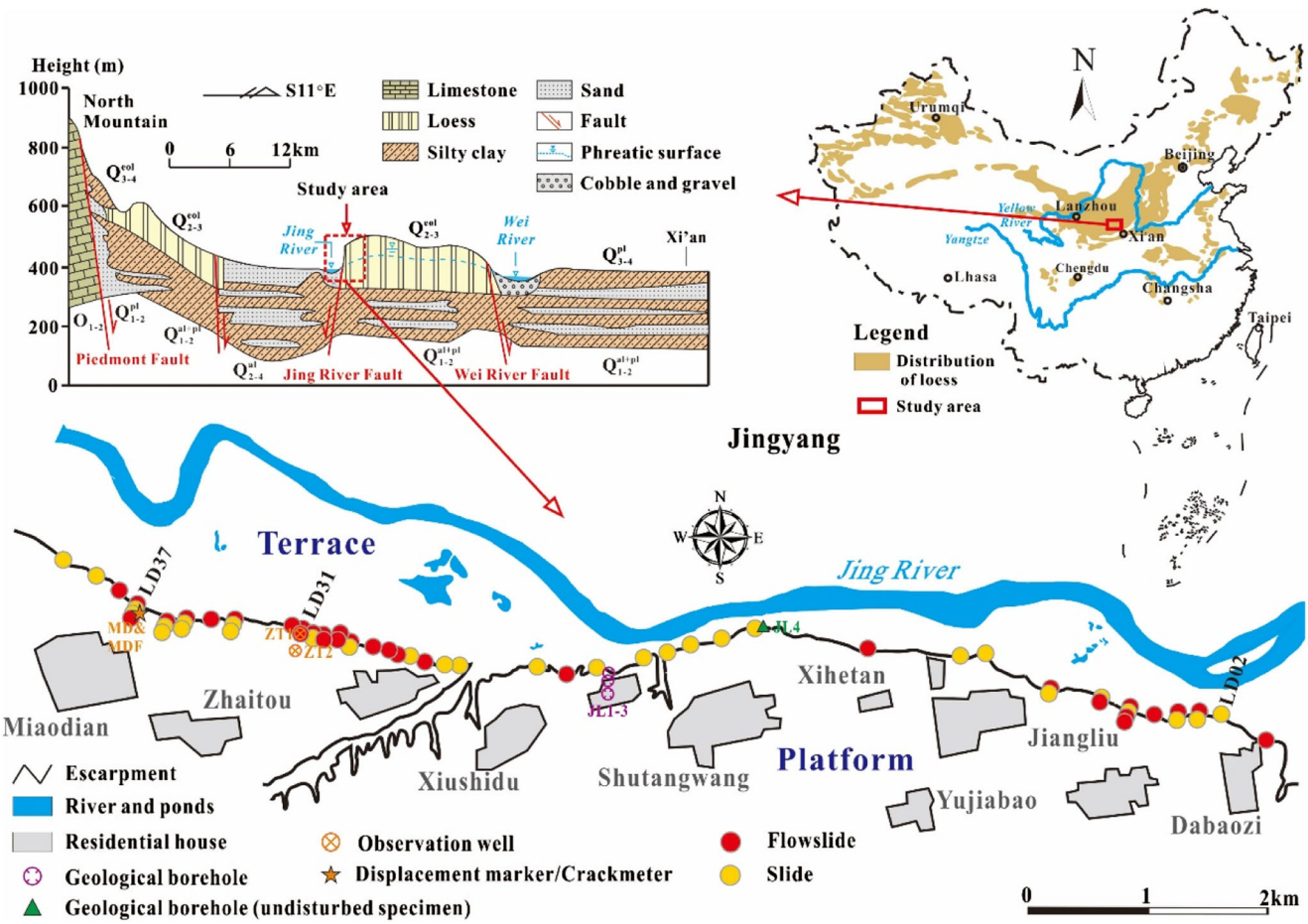

Fig. 1 Geological profile and plan view of the study area

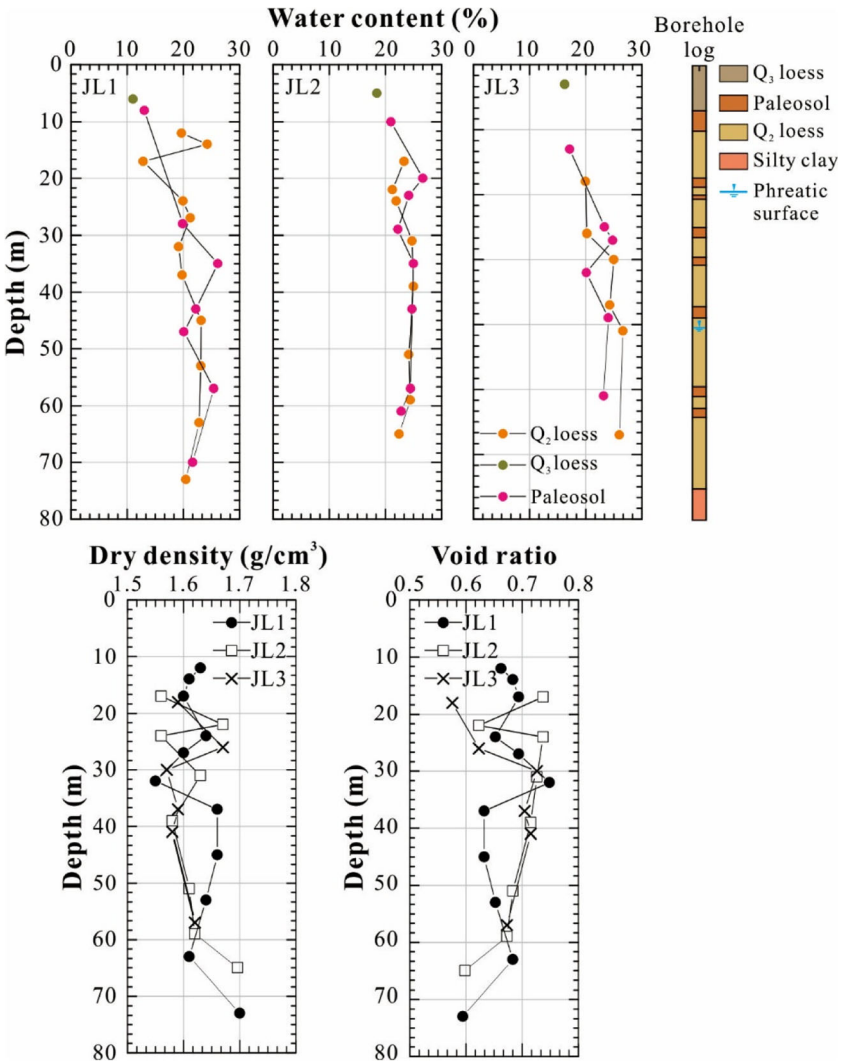

Fig. 2 Variations in water content, dry density, and void ratio against depth. *JL1–3* Geological boreholes in the vicinity of the Jiangliu platform

Figure 2 shows the variations in water content, dry density, and void ratio against depth according to the samples retrieved from three geological boreholes (JL1–3) in the vicinity of Jiangliu. This figure also shows that the water contents initially varied from 10 to 22% and then slightly increased with increasing depth due to the influence of desiccation of the upper crust. It can also be noted from Fig. 2 that the dry densities and void ratios varied within ranges of 1.55–1.7 g/cm^3 and 0.57–0.75, respectively. As intensive irrigation is a common practice in the study area, due to the demands of rural residents for water, the shearing resistance of the loess may be degraded sharply when subjected to irrigation-water infiltration (Melinda et al. 2004; Lu and Likos 2006; Ng et al. 2016). This degradation of strength promotes the development of sliding surfaces. In addition, as the well-developed joint systems in the loess provide additional seepage channels, the fine-grained soils of loess can even be washed away when subjected to large hydraulic gradients, thereby leading to stratum erosion. Stratum erosion, particularly at the toe of slope, can significantly impact slope stability.

Loess landslide types

The loess landslides that have occurred in the study area can be categorized into two types on the basis of the landslide characteristics and topographic investigations, namely, loess flowslide and loess slide (Fig. 3). Loess flowslides behave in a quasi-liquid state that is distinct from similar landslide incidents worldwide; such flowslides can taxi a very long distance at a high velocity (Cascini et al. 2010, 2011; Xu et al. 2013; Oldrich et al. 2014; Leng et al. 2017). The originally deposited strata at shallow depths are likely to be buried below and/or pushed forwards by the landslide deposit, thereby forming a series of thrust structures, as depicted in Fig. 4a, b (Peng 2017, 2018). Liquefaction phenomena due to an inability to dissipate the excess porewater pressure in a very short

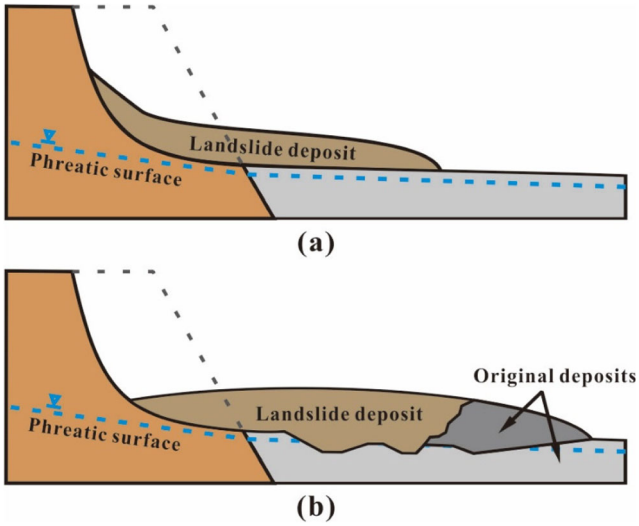

Fig. 3 Loess landslide types: **a** loess slide and **b** loess flowslide

period of sliding can easily be seen at the interface of the landslide deposit and originally deposited strata, as shown in Fig. 4c, d. Compared with loess flowslides, loess slides behave in a quasi-plastic state and taxi a shorter distance.

Loess landslide LD37

A list of all the available records on loess landslides in the south Jingyang platform is provided in Table 1. Due to the completeness of the data available, we selected only loess landslide no. LD37 (Fig. 5) for an in-depth analysis. The landslide characteristic parameters shown in Table 1 are schematically illustrated in Fig. 6. LD37 is characterized by four landslide phases, with the first and final phases classified as the loess flowslide and the second and third phases classified as the loess slide. The H_{max}/L_{max} ratio of LD37 varied from 0.20 to 0.44 for the loess flowslides and from 0.73 to 1.31 for the loess slides where H_{max} corresponds to the distance from platform surface to the bottom of landslide deposit and L_{max} represents the total sliding distance of landslide deposit (equal to $L_s + L_d$, as denoted in Fig. 6). The L_d value varied from 42.8 to 54.7 m for the loess slides and from 130 to 284 m for the loess flowslides, in which L_d indicates the sliding length of landslide deposit on the surface. The triggering mechanism will be discussed in subsequent sections.

Field measurements and laboratory tests

Methodology

To determine the triggering mechanism of a large number of the loess landslides in the study area, we performed field measurements from displacement markers and crackmeters as well as from observation wells despite the time offset between the field measurements and the occurrence of the four landslide phases of LD37. This time offset due to the difficulty in forecasting loess landslides. Despite this time difference, the field measurements of LD37 were analyzed to characterize the evolution of displacements, tension cracks, and phreatic surface and then compared to the results of the triaxial tests that shears a specimen in a drained condition along the constant deviatoric stress path by increasing the back pressure at a constant rate. The results of the triaxial tests on the specimens are listed in Table 2. Insight gained from the comparisons provide crucial evidence revealing the triggering mechanism of the loess landslides in the study area.

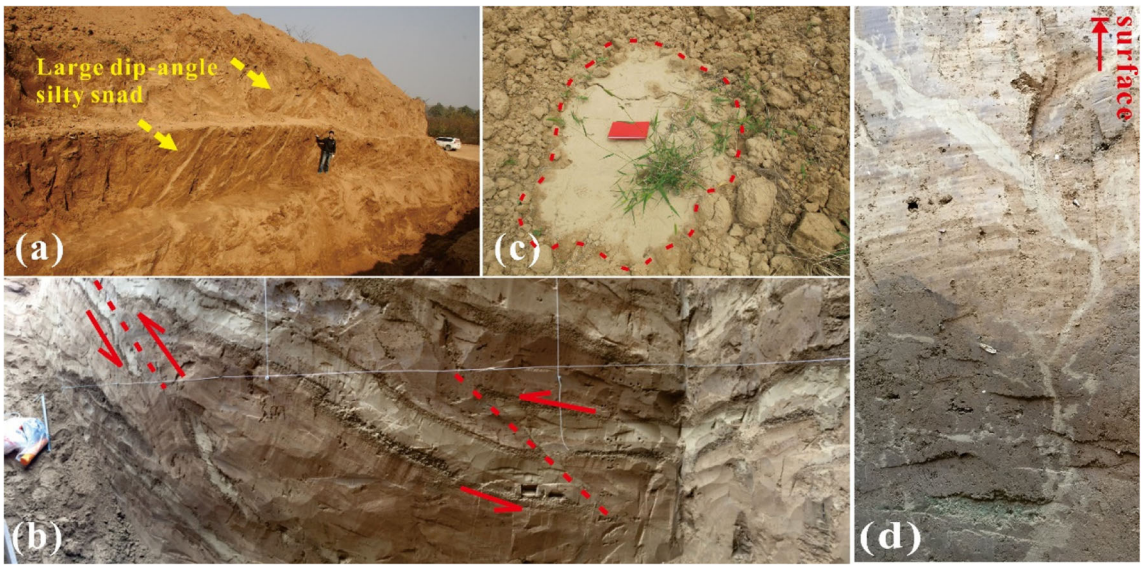

Fig. 4 Photographs of loess strata. **a** Large dip-angle silty sand in trench 1 (shown in Fig. 5), **b** thrust structure in trench 2 (shown in Fig. 5), **c** sand boiling in trench 2 (shown in Fig. 5), **d** liquefaction phenomenon

Table 1 Summary of the loess landslides which have occurred in the south Jingyang platform

Landslide no.	L_d (m)	D_d (m)	W_d (m)	H_{max} (m)	L_{max} (m)	ϕ_α (°)	$V_{deposit}$ (× 10^3 m^3)	Type	Triggered time (year-month-day)
LD1	83.6	20.7	213.3	56.1	117.4	25.5	247.5	Slide	
LD2	47	12.2	96.8	57.2	107.5	28.1	49.6	Slide	
LD3	144.6	7.7	220.4	59.5	210.9	15.7	171	Flowslide	2012-4-10
					92		8	Slide	2012-10
LD4	109.5	19.3	243.5	62.4	169.2	20.2	308.7	Flowslide	1989-8-3
	49.5	6.3	113.4	43.1	109.2	21.5	51.2	Slide	1995-3
LD5	188.6	11.5	148.6	64.3	238.5	15.1	225.6	Flowslide	1990-5
LD6	246.5	4.7	692.6	67.4	241.6	12.8	1128	Flowslide	1984-12-2
	123.2	5.5	692.6	61.6	138.2	24	808	Flowslide	1992-10-15
	209.2	3.2	92.5	61	218	15.6	41	Flowslide	2014-11-28
	204	2.8	69.1	61.6	210	16.3	15	Flowslide	2015-1-15
LD7	172.8	11.2	72.3	62.5	121.8	26.4	83.9	Slide	
	131.7	8.4	131.2	64.7	164.1	21.5	94.3	Flowslide	2012-4-13
				44	98.5		65.2	Flowslide	2014-9-20
LD8	278.7	11.5	514.2	70.4	368.8	9.5	1236	Flowslide	2003-7-23
					27.5		54	Slide	2004
LD9	32.6	16.5	42	65.2	42.6	56.8	15	Slide	
LD10	49.4	10.4	248.6	75.4	118.3	32.5	128	Slide	1997-2
LD11	289	13.7	329	80.7	367	12.4	1303	Flowslide	
LD12	48.5	15.8	228.3	76.5	128.7	30.7	104	Slide	2007
LD13	180.4	22.8	299.8	83.5	256.1	18	863.2	Slide	2005-9-27
LD14	88.7	32.9	306.1	84.8	144.3	30.4	535.9	Slide	
LD15	45	28.2	132.1	63.3	125.1	26.8	100	Slide	
LD16	89.5	19.4	182.3	90.1	131.5	34.4	316	Slide	
LD17	25.6	30.4	218.1	82.3	110.5	36.7	101	Slide	
LD18	365	17.7	248.3	79.9	419	10.8	1604	Flowslide	2001-1-24
LD19	63.9	10	130.4	85.9	144.4	30.7	83	Slide	2005-4
LD20	45.7	4	92.3	49	61	38.8	17	Slide	
LD21	114.9	4.3	109.3	40.9	151.8	15.1	54	Slide	
LD22	140	8	136	54	170	17.6	152	Flowslide	
LD23	79.3	14.9	64.2	44.4	114.8	21.1	76	Slide	
LD24	183.4	10.3	146	53	198.9	14.9	276	Flowslide	
LD25	85	6	40	50	110	24.4	20	Slide	
LD26	158	7	126	54	183	16.4	139	Flowslide	
LD27	314.5	3	181	56.5	369.2	8.7	171	Flowslide	
		18.9	181	52.5	131.2	21.8	449	Slide	
LD28	311.1	4.3	126.8	56.4	410.9	7.8	170	Flowslide	
	167.6	15.5	126.8	52.1	267.4	11	329	Flowslide	
LD29	313.6	3.2		59.4	331.7	10.2	580	Flowslide	1983-3-27
	257.8	14.2		56.2	275.9	11.5	430	Flowslide	2004-3-13
LD30	170	12	227	58	185	17.4	463	Flowslide	
					70.3		210	Slide	
LD31	257.5	5.2	326	60.5	283.2	12.1	436	Flowslide	1985-6
	119.9	12.7	272	55.3	145.6	20.8	415	Flowslide	2004-6
LD32	218	15	190	60	243	13.9	621	Flowslide	1991-3-2
LD33	168.6	4.5	64.4	60	188.9	17.6	350	Flowslide	
	101.7	18.3	64.4	45	122	20.2	120	Slide	
				36	80			Slide	
LD34	202.1	8.5	184.8	48.7	257.4	10.7	190.4	Flowslide	
LD35	233.6	3.6	147.1	47.8	278.4	9.7	124	Flowslide	
	48.5	6.2	147.1	44.2	93.3	25.3	44	Slide	
	45.1	8.8	156.2	44.6	80.4	29	61.9	Slide	2012-3-21
LD36	268.9	9.1	228.6	61.3	298.6	11.6	559	Flowslide	1993-1-15
	127.9	12.6	228.6	52.2	157.6	18.3	369	Slide	
	40.5		141	36	70.2	27.1	42	Slide	
LD37	284	24	162.1	60	305	11.5	350	Flowslide	2013-6-10
	54.7	6.2	106.8	59.5	82	36.8	53	Slide	2013-8
	42.8	3.2	54.6	59	45	53.5	6	Slide	2013-10
	130	21	75.5	60	135	24.4	35	Flowslide	2014-7-26
LD38	279.5	27.5	252.9	57	296.8	10.9	726.1	Flowslide	2015-5-27
LD39	92.5	2.9	98.1	54.3	120.6	24.2	26	Slide	
LD40	69.9	10.8		63.7	110	30.1	114	Slide	

D_d, maximum depth of landslide deposit (m); L_d, sliding distance of landslide deposit on the surface (m); W_d, average width of landslide deposit (m); H_{max}, distance from platform surface to the bottom of landslide deposit (m); L_{max}, total sliding distance of landslide deposit; ϕ_α, value returned by the Arctangent relation between H_{max} and L_{max} (deg.); $V_{deposit}$, volume of landslide deposit (m^3)

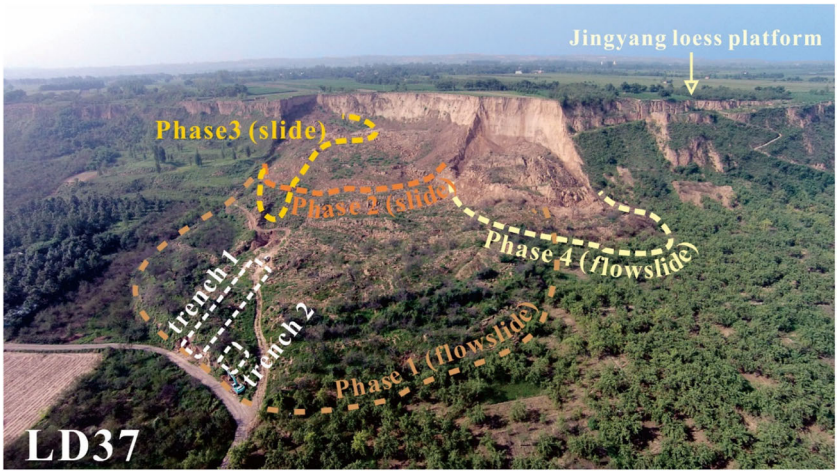

Fig. 5 The four landslide phases of LD37 located in the south Jingyang platform

Displacement measurements

As mentioned, the fine-grained soils of loess can easily be washed away when subjected to significant hydraulic gradients, thereby leading to stratum erosion. Stratum erosion, particularly at the toe of slope, has the potential to lead to slope instability. Some pre-landslide signs, such as displacement and tension crack at the top of the slope due to changes in the hydraulic gradient, can thus be captured prior to the occurrence of loess landslide. Figure 7 shows the extent of four landslide phases and the location of the monitoring instruments for LD37, and Fig. 8 shows the evolution of displacements from locations MD01-03 and MD08-09 for LD37 and the change in phreatic surfaces from ZT1-2 for LD31; however, the data at ZT1-2 were not analyzed due to incompleteness. As can be seen, there was little change at MD01-03 and MD08 during the whole period from June 2016 to June 2018. However, at location MD09, which is connected to the tension cracks, there was initially only a small change, but this subsequently increased dramatically, at which time the four stages can be clearly distinguished, namely, the preliminary stage (Stage 1), the gradual development stage (Stage 2), the rapid development stage (Stage 3), and the final stage (Stage 4). The average horizontal displacement rate increased from 0.2 mm/day in Stage 1 to 0.3 mm/day in Stage 2, while the average vertical displacement rate increased from 0.4 mm/day in Stage 1 to 0.6 mm/day in Stage 2. The average horizontal displacement rate then increased by 0.2 mm/day to 0.5 mm/day in Stage 3, while the average vertical displacement rate increased 0.6 mm/day to 1.2 mm/day in Stage 3. These large changes in average horizontal and vertical displacement rates did not develop any further, however, and fell to 0.005 and 0.07 mm/day, respectively, in Stage 4, indicating that the slope had reached a quasi-steady state.

The evolution of tension crack expansions or contractions from MDF06-07 and MDF12-13 for LD37 is shown in Fig. 9.

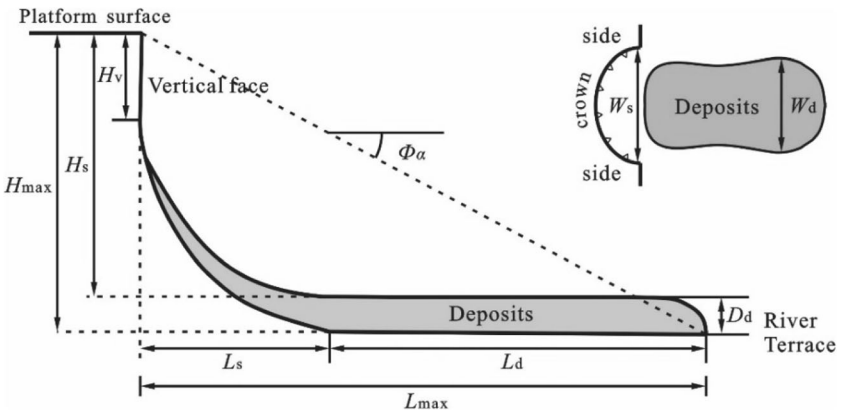

Fig. 6 Schematic illustration of landslide characteristic parameters. D_d Maximum depth of landslide deposit (m), W_d Average width of landslide deposit (m), L_d Sliding distance of landslide deposit on the surface (m), L_s Projected sliding distance of landslide deposit on the sloping ground (m), H_{max} Distance from platform surface to the bottom of landslide deposit (m), H_s Distance from platform surface to the top of landslide deposit (m), L_{max} Total sliding distance of landslide deposit (m); ϕ_α Value returned by the Arctangent relation between H_{max} and L_{max} (deg.); $V_{deposit}$ Volume of landslide deposit (m^3)

Table 2 Basic physical properties of loess

Property	Loess
Specific gravity (Gs)	2.71
Initial moist bulk density (g/cm^3)	1.68
Initial water content (%)	10.5
Initial void ratio	0.78
Liquid limit (%)	26.8
Plastic limit (%)	15.4
Plasticity index (%)	11.4
Horizontal permeability coefficient (10^{-4} cm/s)	1.85
Vertical permeability coefficient (10^{-4} cm/s)	2.92

At location MDF13, the tension crack first expanded at a rate of 0.25 mm/day and then contracted at a rate of 0.01 mm/day.

CSD triaxial tests

The CSD triaxial test was employed to investigate the behavior of loess in terms of the effect of the rising phreatic surface. Cylindrical specimens of 39.1 mm in diameter and 80 mm in height were retrieved from the geological borehole JL4 depicted in Fig. 1, and CSD tests were performed on loess specimens collected at borehole depths of 6, 12, and 24 m, respectively. CO_2 was introduced in the saturation phase to displace air from the specimens, thereby allowing for back pressure saturation to be performed. All specimens were saturated to a value of $B \geq 0.95$ (Skempton 1954). The consolidation pressures were obtained by increasing cell pressure and axial load, and $K_0 = 0.5$, earth pressure coefficient at rest corresponding to the ratio of the horizontal effective stress, σ'_h, to the vertical effective stress, σ'_v, was adopted. The specimens were then sheared in a drained condition along the constant deviatoric stress path by increasing the back pressure u at a rate of 1 kPa/h. The results of the CSD tests are given in Fig. 10 in terms of axial strain (ε_a) versus mean stress (p'), volumetric strain (ε_v) versus mean stress (p'), and deviatoric stress (q') versus mean stress (p'), in which $p' = (\sigma_1' + 2\sigma_3')/3$ and $q' = \sigma_1' - \sigma_3'$.

Analysis and discussion

The horizontal and vertical displacement rates shown in Fig. 8 were measured in Stage 2 at location MD09 and averaged up to 0.3 and 0.6 mm/day, respectively. Despite

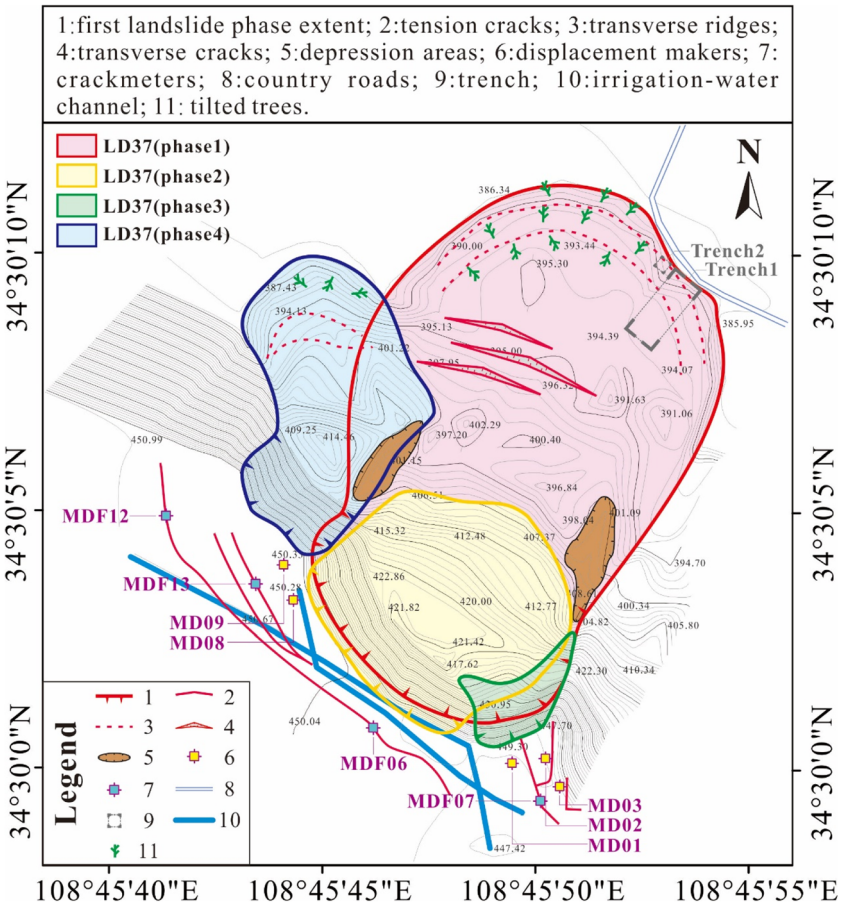

Fig. 7 Extent of four landslide phases and location of monitoring instruments for LD37

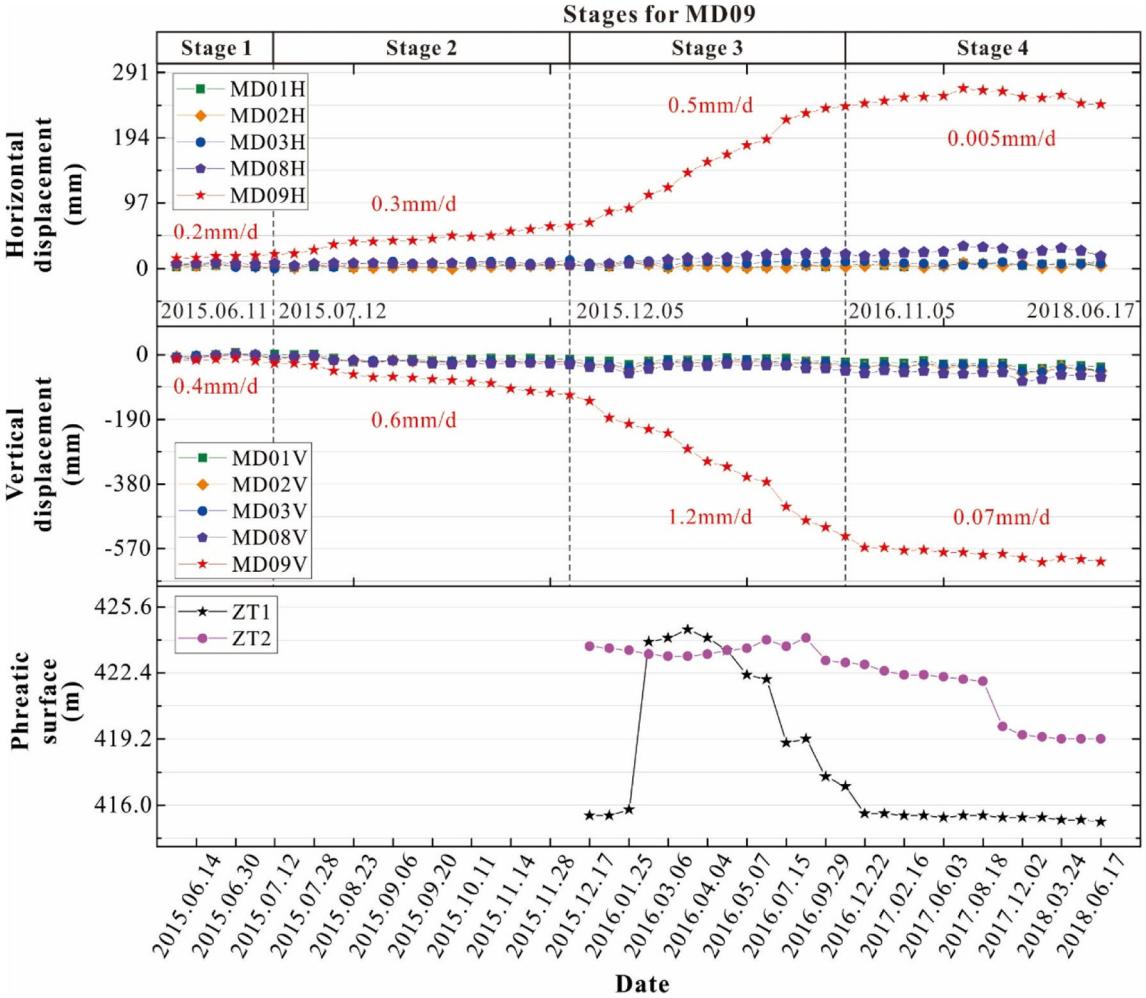

Fig. 8 Evolution of displacements from MD01-03 and MD08-09 for LD37 and change in phreatic surfaces from ZT1-2 for LD31. See Fig. 7 for locations

the lack of porewater pressure records, it can be inferred that the seepage induced by irrigation-water infiltration from the top of the slope through joints and/or fractures towards the toe led to washing away of the fine-grained

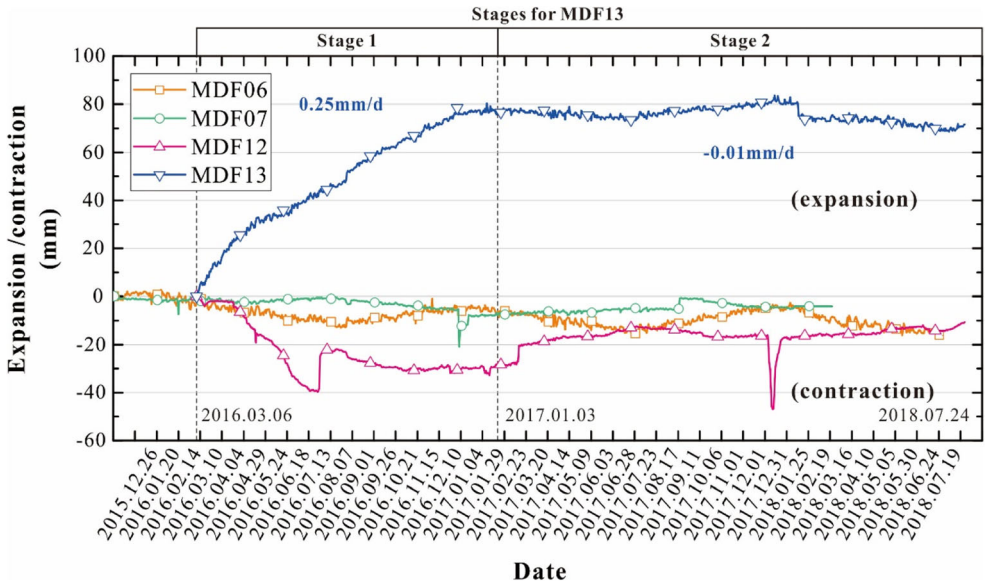

Fig. 9 Evolution of tension cracks from MDF06-07 and MDF12-13 for LD37

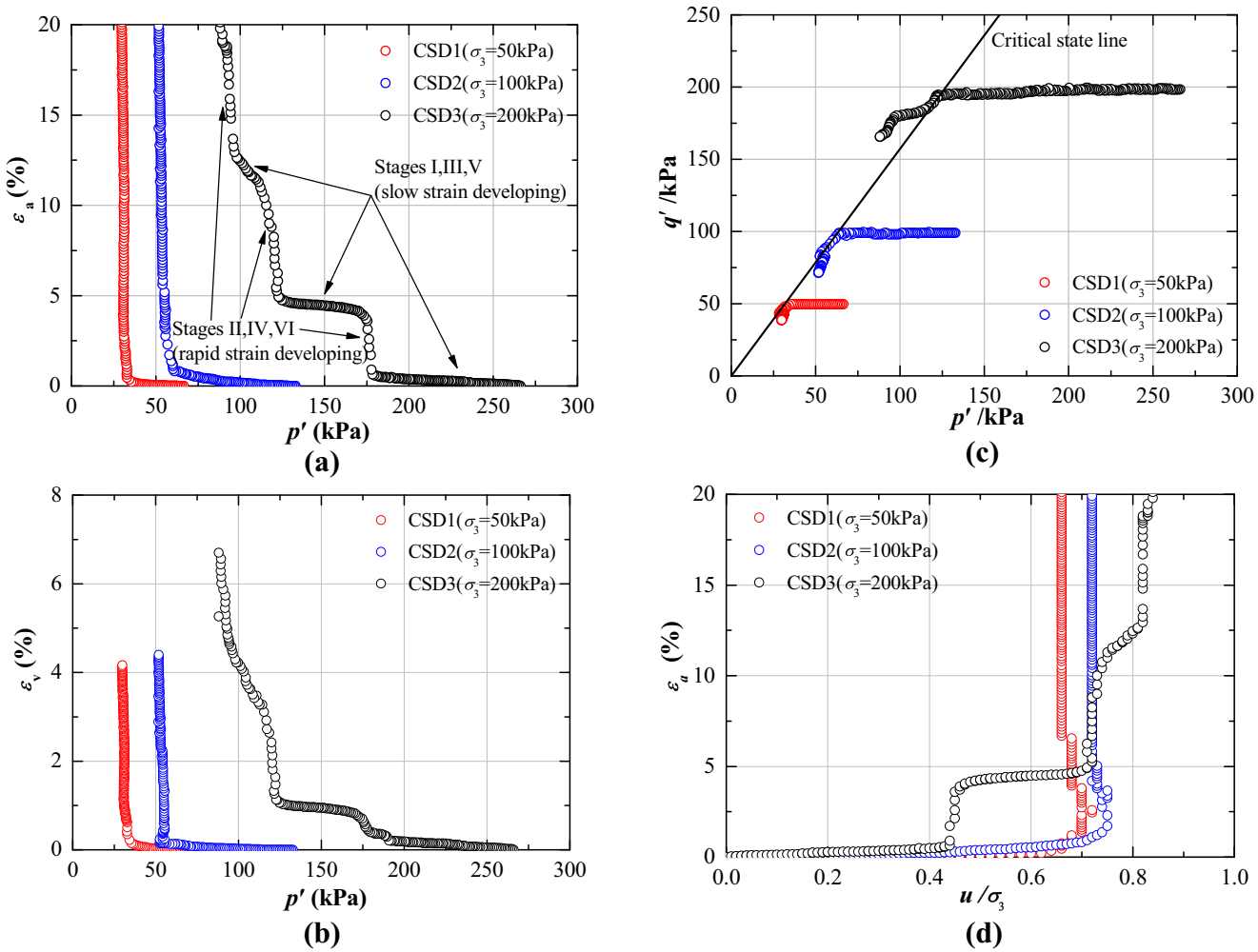

Fig. 10 Results of constant shear drained (CSD) triaxial tests: **a** ε_a (axial strain) vs. p'(mean stress), **b** ε_v (volumetric strain) vs. p'(mean stress), **c** q' (deviatoric stress) vs. p'(mean stress), **d** ε_a (axial strain) vs. u (porewater pressure)/σ_3

soils (see the reeds growing up at the toe of LD37 in Fig. 11) and the subsequent downwards movement of the slope in a gentle manner, initiating a series of local sliding surfaces. In Stage 3, the average horizontal and vertical displacement rates were measured at values of 0.5 and 1.2 mm/day, respectively; these were nearly two-fold higher than those in the previous stage and indicated a further development of the local sliding surfaces associated with a more severe stratum erosion of the fine-grained soils. However, thereafter, in Stage 4, the average horizontal and vertical displacement rates showed a large decline 0.005 and 0.07 mm/day, respectively. From these data, it can be postulated that the effect of particle rearrangement and/or particle inter-locking at the local sliding surfaces effectively impeded subsequent movement of the slope. In some cases, depending upon

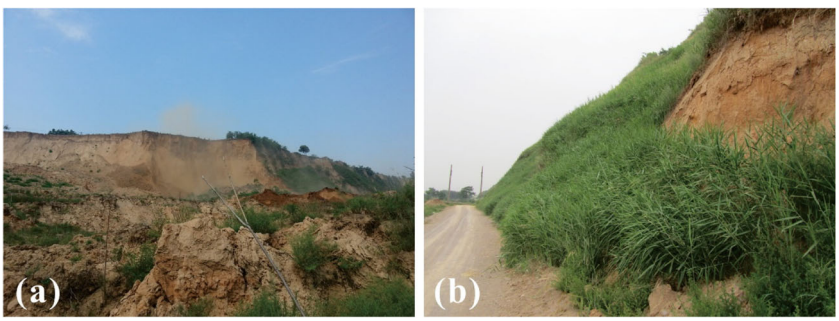

Fig. 11 Photos showing reeds growing at the toe of LD37. **a** Whole view of LD37, **b** enlargement of the toe area

the severity of stratum erosion, the movement of the slope may develop further, ultimately triggering a landslide incident.

At location MDF13, the tension crack dramatically expanded in Stage 1, at a rate of 0.25 mm/day, then contracted to a rate of −0.01 mm/day in Stage 2, as shown in Fig. 9. Stages 1 and 2 at MDF13 showed a pattern similar to that at MD09 in Stages 3 and 4. This consistency validates the field measurements.

It can be seen from Fig. 10 that the axial strain ε_a and volumetric strain ε_v changed only slightly during a steady reduction in the effective mean stress p', while the deviatoric stress remained constant. This phenomenon is due to the back pressure u not being sufficiently high to make the soil skeleton unstable, yet high enough to be capable of initiating local failure surfaces. The shearing resistance available along the local failure surfaces prevented the axial strain ε_a or volumetric strain ε_v from growing. As the back pressure u increased to a level high enough to cause the soil skeleton to become unstable, the axial strain ε_a and volumetric strain ε_v also substantially increased, indicating that the loess specimen sheared along the local failure surfaces where the soil particles had been rearranged. Since the soil skeleton remains stable when subjected to small back pressures or the effect of particle rearrangement and inter-locking and became unstable when subjected to high back pressures, u outweighed the effect of particle rearrangement. The developing slow strain–rapid strain cycle can be repeatedly seen in the ε–p' plot. At CSD3, this developing slow strain–rapid strain cycle was repeated three times, while at CSD1-2, it was seen only once. As the back pressure u increased sufficiently to cause local failure surfaces to be elongated and to become connected with each other to form a global failure surface, the specimen failed as the shearing resistance along the global failure surface ran; at CSD1-2, the ratio of the back pressure u to the cell pressure σ_3' reached 0.7, while at CSD3, it approached 0.8. It is evident that the effect of particle rearrangement and inter-locking enabled the soil skeleton to sustain larger back pressures and/or impeded the development of global failure surface.

The triggering mechanism of the loess landslides in the study area can be summarized as follows. Since the phreatic surface was raised by 13–37 m between 1976 and 1992 and no loess landslides were reported before agricultural irrigation, the loess landslides were most likely triggered by induced seepage of irrigation-water infiltration from the top of the slope through joints towards the toe. Consequently, subjected to a seepage force that was greater than the shear strength of loess, the fine-grained soils were washed away, leading to stratum erosion. This stratum erosion, particularly at the toe of slope, greatly impacted slope stability and initiated a series of local sliding surfaces, with the negligible displacement rates shown in Stages 1 and 2 at MD09 (Fig. 8); this development is different from the CSD triaxial tests undertaken where the local failures were initiated by introducing the back pressure u to the specimen. Although the CSD triaxial test is not capable of taking the effect of stratum erosion into account, its results do reflect the initiation of the local failures by the axial strains ε_a (or volumetric strains ε_v) developing at a slow pace, as shown in Stages I, III, and V of CSD3 and Stages I, III, and V of CSD3, and can thus be compared to those at Stages 1 and 2 at MD09.

When subjected to an even greater seepage force, the stratum erosion became more severe and led to instability of the soil skeletons and further development of local sliding surfaces. The slope moved downwards at horizontal and vertical displacement rates that were nearly twofold higher than those in the previous stage, as shown in Stage 3 of MD09. By introducing higher back pressures to the specimen, the CSD triaxial test linked a further development of the local failures to the axial strains ε_a (or volumetric strains ε_v) at a rapid pace, as shown in Stages II, IV, and VI of CSD3; therefore, Stages II, IV, and VI of CSD3 can correspond to Stage 3 of MD09.

The developing slow strain–rapid strain cycles in the ε–p' plot of the CSD triaxial test also indicated that the loess landslides in the study area were a feature of the progressive failure. It is recognized that the severity of stratum erosion determines whether local sliding surfaces can develop into a global sliding surface (Xu et al. 2013; Zhang and Wang 2018). Moreover, although the loess landslides were not triggered by the raising of the phreatic surface, but rather by the seepage induced by irrigation water, the former greatly weakened the available shearing resistance along the local sliding surfaces, thereby increasing the potential of loess landslide. Preventive measures to reduce water infiltration into loess slope should be taken along with the effective management of agricultural irrigation to prevent future similar incidents from reoccurring.

Conclusions

This paper presented the results of an investigation into the loess landslide LD37 for a better understanding of the triggering mechanism of the loess landslides in the study area. Based upon the results and discussions, the following conclusions can be drawn:

(1) The field measurements on LD37 and the CSD triaxial test results were analyzed. Insights gained from the comparisons of the LD37 field measurements and the CSD triaxial test results with real phenomena indicated that irrigation-water infiltration induced seepage from the top of slope through joints and/or fractures towards the toe and that this seepage can be considered to be the major contributor to the triggering of the loess landslides in the study area.

(2) The seepage washed the fine-grained soils away when the seepage force was greater than the shear strength of loess, thereby leading to stratum erosion and, consequently an unstable soil skeleton. Ultimately, the unstable slope started to move downwards, initiating the local sliding surfaces, with the small displacement rates as shown in Stages 1 and 2 at MD09. Although the effect of stratum erosion cannot be taken into account in the CSD triaxial test, the test did capture the initiation of the local failures by the axial strain ε_a (or volumetric strain ε_v) which developed at a slow pace, as shown in Stages I, III, and V at CSD3.

(3) When subjected to an even greater seepage force, stratum erosion became more severe, which not only led to an unstable soil skeleton, but also indicated a further development in the local sliding surfaces. The slope thus moved downwards at displacement rates that were nearly twofold higher than those during the previous stage, as shown in Stage 3 of MD09. The results of the CSD triaxial test linked the further development of the local failures with the axial strain ε_a (or volumetric strain ε_v) that developed at a rapid pace, as shown in Stages II, IV, and VI of CSD3.

(4) The development of slow strain–rapid strain cycles in the $\varepsilon - p'$ plot from the CSD triaxial test results implied that the loess landslides which occurred in the study area were a feature of this progressive failure. Preventive measures to reduce the irrigation-water infiltration into loess slope should be taken along with the effective management of agricultural irrigation to avoid similar incidents in the future.

Acknowledgements This study would not have been possible without financial supports from the Natural Science Foundation of China under Grant Nos. 41702298, 41790442 and 41877289 and from the Natural Science Basic Research Plan in Shaanxi Province of China under Grant No. 2017JQ4020, and Open Fund of Shandong Provincial Key Laboratory of Depositional Mineralization & Sedimentary Minerals under Grant Nos. DMSM2017029. The authors would like to express their sincere gratitude for the technical support provided by Professor Fu-Chu Dai and Dr. Zhi-Qiang Zhao at Beijing University of Technology.

References

Cascini L, Cuomo S, Pastor M, Sorbino G (2010) Modeling of rainfall-induced shallow landslides of the flow-type. J Geotech Geoenviron 136(1):85–98

Cascini L, Cuomo S, Della Sala M (2011) Spatial and temporal occurrence of rainfall-induced shallow landslides of flow type: a case of Sarno-Quindici, Italy. Geomorphology 126:148–158

Cheng WC, Ni JC, Shen SL (2017a) Experimental and analytical modeling of shield segment under cyclic loading. Int J Geomech 17(6): 04016146

Cheng WC, Ni JC, Shen SL, Huang HW (2017b) Investigation into factors affecting jacking force: a case study. Ice Proc Geotech Eng 170(4):322–334

Cheng WC, Ni JC, Arulrajah A, Huang HW (2018a) A simple approach for characterising tunnel bore conditions based upon pipe-jacking data. Tunn Undergr Space Technol 71:494–504

Cheng WC, Ni JC, Shen JS, Wang ZF (2018b) Modeling of permeation and fracturing grouting in sand: laboratory investigations. J Test Eval. https://doi.org/10.1520/JTE20170170

Cheng WC, Song ZP, Tian W, Wang ZF (2018c) Shield tunnel uplift and deformation characterisation: A case study from Zhengzhou metro. Tunn Undergr Space Technol 79:83–95

Cheng WC, Ni JC, Huang HW, Arulrajah A (2018d) The use of tunnelling parameters and spoil characteristics to assess soil types: A case study from alluvial deposits at a pipejacking project site. Bull Eng Geol Environ. https://doi.org/10.1007/s10064-018-1288-4

Derbyshire E (2001) Geological hazards in loess terrain, with particular reference to the loess regions of China. Earth Sci Rev 54:231–260

Derbyshire E, Dijkstra TA, Smalley IJ, Li YJ (1994) Failure mechanisms in loess and the effects of moisture content changes on remolded strength. Quat Int 24:5–15

Du YJ, Jiang NJ, Liu SY, Jin F, Singh DN, Pulppara A (2014a) Engineering properties and microstructural characteristics of cement solidified zinc-contaminated kaolin clay. Can Geotech J 51:289–302

Du YJ, Wei ML, Reddy KR, Liu ZP, Jin F (2014b) Effect of acid rain pH on leaching behavior of cement stabilized lead-contaminated soil. J Hazard Mater 271:131–140

Fell R, Glastonbury J, Hunter G (2007) Rapid landslides: the importance of understanding mechanisms and rupture surface mechanics. Q J Eng Geol Hydrogeol 40(1):9–27

Lai JX, Qiu JL, Fan HB, Zhang Q, Hu ZN, Wang JB, Chen JX (2016) Fiber bragg grating sensors-based in situ monitoring and safety assessment of loess tunnel. J Sens 2016:1–12

Lai JX, He SY, Qiu JL, Chen JX, Wang LX, Wang K, Wang JB (2017) Characteristics of earthquake disasters and aseismic measures of tunnels in Wenchuan earthquake. Environ Earth Sci 76(2):76–94

Leng YQ, Peng JB, Wang QY, Meng ZJ, Huang WL (2017) A fluidized landslide occurred in the loess plateau: a study on loess landslide in south Jingyang tableland. Eng Geol 236:129–136

Liu NN, Huang QB, Fan W, Ma YJ, Peng JB (2018) Seismic responses of a metro tunnel in a ground fissure site. Geomechanics and Engineering 15:775–781. https://doi.org/10.1007/s10064-018-01432-8

Lu N, Likos W (2006) Suction stress characteristic curve for unsaturated soil. J Geotech Geoenviron 132(2):131–142

Melinda F, Rahardjo H, Han KK, Leong EC (2004) Shear strength of compacted soil under infiltration condition. J Geotech Geoenviron 130(8):807–817

Ng CWW, Sadeghi H, Jafarzadeh F (2016) Compression and shear strength characteristics of compacted loess at high suctions. Can Geotech J 54:690–699

Oldrich H, Serge L, Luciano P (2014) The Varnes classification of landslide types, an update. Landslides 11:167–194

Peng JB, Fan ZJ, Wu D, Zhuang JQ, Dai FC, Chen WW, Zhao C (2015) Heavy rainfall triggered loess-mudstone landslide and subsequent debris flow in Tianshui, China. Eng Geol 186:79–90

Peng JB, Wang GH, Wang QY, Zhang FY (2017) Shear wave velocity imaging of landslide debris deposited on an erodible bed and possible movement mechanism for a loess landslide in Jingyang, Xi'an, China. Landslides 14:1503–1512

Peng JB, Ma PH, Wang QY, Zhu XH, Zhang FY, Tong X, Huang WL (2018) Interaction between landsliding materials and the underlying erodible bed in a loess flowslide. Eng Geol 234:38–49

Qiu JL, Wang XL, He SY, Liu HQ, Lai JX, Wang LX (2017) The catastrophic landside in Maoxian County, Sichuan, SW China on June 24. Nat Hazards 89(3):1485–1493

Qiu JL, Wang XL, Lai JX, Zhang Q, Wang JB (2018) Response characteristics and preventions for seismic subsidence of loess in Northwest China. Nat Hazards 92(3):1909–1935

Shen SL, Xu YS (2011) Numerical evaluation of land subsidence induced by groundwater pumping in Shanghai. Can Geotech J 48(9):1378–1392

Shen SL, Ma L, Xu YS, Yin ZY (2013) Interpretation of increased deformation rate in aquifer IV due to groundwater pumping in Shanghai. Can Geotech J 50(11):1129–1142

Shen SL, Wang ZF, Cheng WC (2017) Estimation of lateral displacement induced by jet grouting in clayey soils. Geotechnique 67(7):1–10

Skempton AW (1954) The Pore-Pressure Coefficients and GÃ©otechnique 4(4):143–147

Wang JJ, Liang Y, Zhang H, Wu Y, Lin X (2014) A loess landslide induced by excavation and rainfall. Landslides 11:141–152

Wang ZF, Shen JS, Cheng WC (2018a) Simple Method to Predict Ground Displacements Caused by Installing Horizontal Jet-Grouting Columns. Math Probl Eng 2018:1–11

Wang ZF, Cheng WC, Wang YQ, Du JQ (2018b) Simple Method to Predict Settlement of Composite Foundation under Embankment. Int J Geomech 18(12):04018158

Wu YX, Shen SL, Xu YS, Yin ZY (2015) Characteristics of groundwater seepage with cutoff wall in gravel aquifer. I: field observations. Can Geotech J 52(10):1526–1538

Wu YX, Shen SL, Yuan DJ (2016) Characteristics of dewatering induced drawdown curve under blocking effect of retaining wall in aquifer. J Hydrol 539:554–566

Wu YX, Shen SL, Cheng WC, Hino T (2017) Semi-analytical solution to pumping test data with barrier, wellbore storage, and partial penetration effects. Eng Geol 226:44–51

Xu L, Dai FC, Tu XB, Javed I, Woodard MJ, Jin YL, Tham LG (2013) Occurrence of landsliding on slopes where flowsliding had previously occurred: an investigation in a loess platform, north-West China. Catena 104:195–209

Xu YS, Ma L, Du YJ, Shen SL (2012) Analysis on urbanization induced land subsidence in Shanghai. Nat Hazards 63(2):1255–1267

Xu YS, Shen SL, Ma L, Sun WJ, Yin ZY (2014) Evaluation of the blocking effect of retaining walls on groundwater seepage in aquifers with different insertion depths. Eng Geol 183:254–264

Xu YS, Shen SL, Ren DJ, Wu HN (2016) Factor analysis of land subsidence in Shanghai: a view based on strategic environmental assessment. Sustainability 8:573 (1-12)

Xu ZJ, Lin ZG, Zhang MS (2007) Loess in China and loess landslides. Chin J Rock Mech Eng 26:1297–1312 (in Chinese)

Zhang MS, Liu J (2010) Controlling factors of loess landslides in western China. Environ Earth Sci 59:1671–1680

Zhang FY, Wang GH (2018) Effect of irrigation-induced densification on the post-failure behavior of loess flowslides occurring on the Heifangtai area, Gansu, China. Eng Geol 236:111–118

Zhang D, Wang G, Luo C, Chen J, Zhou Y (2009) A rapid loess flowslide triggered by irrigation in China. Landslides 6:55–60

Zhang FY, Wang GH, Toshitaka K, Chen WW, Zhang DX, Yang J (2013) Undrained shear behavior of loess saturated with different concentrations of sodium chloride solution. Eng Geol 155:69–79

Zhang FY, Wang GH, Toshitaka K, Chen WW (2014) Effect of porewater chemistry on undrained shear behaviour of saturated loess. Q J Eng Geol Hydrogeol 47:201–210

Zhang FY, Kang C, Chan D, Zhang XC, Pei XJ, Peng JB (2017) A study of a flowslide with significant entrainment in loess areas in China. Earth Surf Process Landf 42(14):2295–2305

Zhao CY, Zhang Q, He Y, Peng JB, Yang CS, Kang Y (2016) Small-scale loess landslide monitoring with small baseline subsets interferometric synthetic aperture radar technique—case study of Xingyuan landslide, Shaanxi, China. J Appl Remote Sens 10:26–30

Zhou JX, Zhu CY, Zheng JM, Wang XH, Liu ZH (2002) Landslide disaster in the loess area of China. J For Res 13:157–161

Zhuang JQ, Peng JB, Wang GH, Iqbal J, Wang Y, Li W (2017) Distribution and characteristics of landslide in loess plateau: a case study in Shaanxi province. Eng Geol 236:89–96